11th International Symposium on Turbulence and Shear Flow Phenomena (TSFP11)
Southampton, UK, July 30 to August 2, 2019

EFFECTS OF PRESSURE GRADIENTS AND STREAMLINE CURVATURE ON THE STATISTICS OF A TURBULENT PIPE FLOW

Liuyang Ding
Department of Mechanical and Aerospace Engineering
Princeton University
Princeton, NJ 08544, USA
liuyangd@princeto.edu

Theresa Saxton-Fox*
Department of Mechanical and Aerospace Engineering
Princeton University
Princeton, NJ 08544, USA
tsaxton@gmail.com

Marcus Hultmark
Department of Mechanical and Aerospace Engineering
Princeton University
Princeton, NJ 08544, USA
hultmark@princeton.edu

Alexander Smits
Department of Mechanical and Aerospace Engineering
Princeton University
Princeton, NJ 08544, USA
asmits@princeton.edu

ABSTRACT

The mean velocity and Reynolds shear stress distributions in a turbulent pipe flow past a streamlined axisymmetric body were examined using particle image velocimetry. Here, we report the behavior in the bow region of the body where the flow experiences a favorable pressure gradient and convex curvature, as well as the subsequent flow recovery behavior over the constant cross-sectional area midsection of the body. Three body diameters were chosen to provide pressure gradients and streamline curvature of different magnitudes. In the bow section, the mean streamwise velocity followed a linear distribution in the region above the overlap layer of the pipe wall. The formation of the linear profiles was explained by examining the Reynolds shear stress, which indicated strong momentum transfer near the body surface in the direction opposite to that near the pipe surface. This momentum transfer was initiated by flow deceleration and streamline divergence in the region just upstream of the bow tip. The severity of these processes increased with the size of the body. In the constant area recovery section, noticeable variations were observed near walls, but overall the flow remained far from equilibrium, and the recovery appeared to be very slow.

INTRODUCTION

Wall-bounded turbulence subjected to non-equilibrium conditions is widely encountered in practical flows, and significantly affects the performances of many fluid dynamic devices. However, our understanding of such flows is limited – there is no general framework to extend our knowledge on canonical wall-bounded turbulence (constrained by parallel walls or a flat plate) to flows experiencing changing boundary conditions. In particular, when there are curved boundaries and/or non-constant cross-sectional areas, pressure gradients and streamline curvature play important roles in turbulence production, dissipation and transport. For flows under these conditions, the extent to which our knowledge on scaling laws, coherent structures and physical models need to be modified is of great interest; existing models for Reynolds-averaged Navier-Stokes (RANS) simulation and Large-eddy simulation (LES) need to be validated through experimental studies.

Past studies have revealed some effects of favorable pressure gradients (FPG) and adverse pressure gradients (APG) on the mean velocity and turbulence intensity of wall-bounded flows. When the pressure gradient changes from FPG ($dp/dx < 0$) to APG ($dp/dx > 0$) (for pipe and channel flows, dp/dx here is the net pressure gradient after subtracting the part balancing the wall friction), the slope of the log-law region increases (Spalart & Watmuff, 1993; Nagib & Chauhan, 2008). In the wake region, APG tends to amplify the deviation from the log law and shorten the extent of the log-law region (Monty *et al.*, 2011). For the influence of pressure gradients on turbulence intensity, some insights can be gained by examining additional production terms besides $-\overline{uv}\frac{dU}{dy}$. For instance, $-\overline{u^2}\frac{dU}{dx}$ is positive when $dp/dx > 0$ and negative when $dp/dx < 0$, leading to turbulence being energized and suppressed under APG and FPG, respectively. Such effects have been widely observed in experiments, as in Harun *et al.* (2013); Nagano *et al.* (1993).

The effects of streamline curvature have also been investigated experimentally, notably by Muck *et al.* (1985) and Hoffmann *et al.* (1985), who concluded that convex curvature 'stabilized' (attenuated) turbulence whereas concave curvature 'destabilized' (amplified) turbulence. Similar effects were also observed by Smits *et al.* (1979) in boundary layer flows subjected to impulses formed by short regions of wall curvature. In particular, Smits *et al.* (1979) discovered a non-monotonic recovery (second-order response) of turbulence to the equilibrium state, which is now recog-

*Present affiliation: Department of Aerospace Engineering University of Illinois at Urbana-Champaign, Urbana, IL 61801

nized as representative of a variety of non-equilibrium turbulence undergoing recovery processes. See, for example, Van Buren *et al.* (2019); Smits *et al.* (2019); Saxton-Fox *et al.* (2019).

In the present work, a fully developed turbulent pipe flow is perturbed by a streamlined axisymmetric body placed on the centerline, introducing a spatially-varying pressure gradient and streamline curvature. We will examine the response of the flow to combined pressure and curvature effects, as well as the recovery behavior downstream.

EXPERIMENT

Figure 1 illustrates the test configuration. A streamlined axisymmetric body was placed on the centerline of a pipe that has an inner diameter of $D = 2R = 38.1$ mm. The body consisted of three sections – the bow ($0< x/R <2.67$), stern ($10< x/R <12.67$) and cylindrical recovery ($2.67< x/R <10$) sections. The bow section is a prolate spheroid; the contour of the stern follows a 4th-order power law to minimize the drag (Moonesun *et al.*, 2017). With the presence of the body, the incoming flow experienced FPG and convex curvature over the bow, followed by relaxation in the recovery section, and then entered the stern region with APG and convex curvature. Three body diameters, $d = D/3$, $\sqrt{2}D/3$ and $\sqrt{3}D/3$, were chosen to vary the magnitude and rate of change of pressure and curvature, where d is the diameter of the body of revolution. The inflow was ensured to be fully developed by allowing a development length of $200D$ upstream of the body.

We conducted planar particle image velocimetry (PIV) in the axial-radial plane to study the evolution of turbulence. As depicted in figure 2, two cameras (LaVision Imager sCMOS) with an offset in the axial direction were positioned on opposite sides of the pipe to simultaneously achieve high spatial resolution and an extended field of view. A 2x teleconverter (Vivitar) was attached to each camera to further enhance the resolution, leading to a magnification of 0.54 (83 pix/mm). Data were taken at two axial locations covering the bow section plus approximately half of the recovery section. A water-filled box was sealed around the pipe to alleviate image distortion due to unmatched index of refraction. The body in our experiment was supported by an airfoil-shaped (NACA0015) sting attached to a pipe insert. We chose our field of view to be the top half of the pipe while the sting was positioned at the bottom ensuring minimum influence to the flow. The pipe insert had an inner diameter matching that of the glass pipe, and was housed in a joint block connecting the upstream and downstream pipe sections. The pipe facility operated at a bulk velocity $U_b \approx 4.1$ m/s for the upstream fully developed flow, corresponding to $Re_D = U_b D/\nu \approx 156{,}000$, where $\nu = 10^{-6}$ is the kinematic viscosity of water at 20 °C. Using the friction

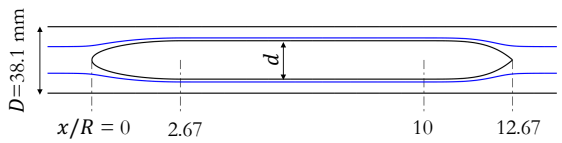

Figure 1: Test section geometry. Three body diameters were tested, i.e. $d = D/3$, $\sqrt{2}D/3$ and $\sqrt{3}D/3$. Blue solid lines are selected streamlines from a potential flow simulation. Flow is from left to right.

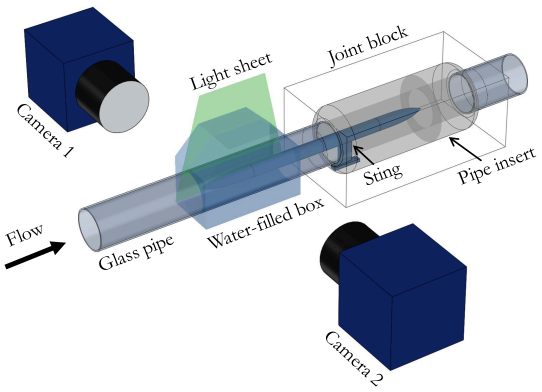

Figure 2: Schematic of the experimental setup.

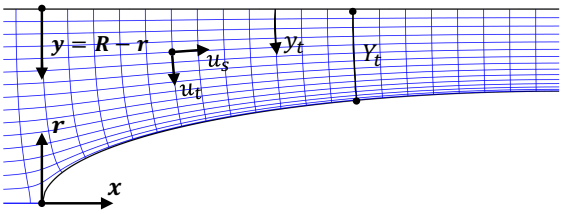

Figure 3: Streamline coordinate system and notations. Flow is from left to right.

factor correlation reported by McKeon *et al.* (2004), we obtained the upstream friction velocity, $u_\tau = 0.186$ m/s, and $Re_\tau = u_\tau R/\nu = 3550$.

For each of the three bodies used here, 20,000 image pairs were processed to calculate mean statistics. Particle tracking analysis was performed with an in-house code that tracks matched particle pairs using a non-iterative histogram-based algorithm (Fuchs *et al.*, 2017). Particle tracking was done first in the image space, and displacement vectors were mapped to the physical space to calculate velocity. This was to eliminate errors associated with interpolation of pixel intensities during dewarping. Mean velocity and Reynolds stresses at each grid point were then calculated by averaging quantities of individual particles within a small volume (Kähler *et al.*, 2012; Agüera *et al.*, 2016). The final spatial resolution is 0.8×0.4 mm^2.

RESULTS

Streamline coordinate system

As the flow was constrained by two surfaces (pipe and body) that were not parallel, we examined the evolution of turbulence statistics in a streamline coordinate system generated using OpenFOAM (v6). The notations are defined in figure 3: subscripts 's' and 't' (e.g. u_s and u_t) denote quantities in the streamline and potential line directions, respectively, where positive u_t points toward the body surface. Also, y_t starts from the pipe wall and is the coordinate along each potential line, and Y_t is the total length of a potential line, which decreases in the axial direction until the recovery section. In addition, x, r and $y = R - r$ are the axial, the radial and the wall-normal (pipe wall) directions, as usual, and $x = 0$ is at the tip of the bow.

To see the extent to which streamlines of the potential flow represent the true turbulence mean flow, we ex-

amined the ratio between U_s and U_t (hereafter, we will use Reynolds decomposition, $u = U + u'$). It turned out that U_t/U_s is below 3%, indicating the mean flow only slightly deviates from the potential flow streamlines.

Bulk acceleration and streamline curvature

Based on the geometry of the bodies and the conservation of mass, we can calculate $U_b(x)$ at any axial location. The acceleration factor in terms of U_b, i.e. $K_b = \frac{\nu}{U_b^2}\frac{dU_b}{dx}$, is plotted in figure 4. It may be seen that K_b at $x = 0$ for the three bodies varies approximately in the ratio 1:2:3, that is, it scales approximately with d^2. However, the largest body creates a non-monotonic K_b peaking at $x/R \approx 0.6$, while for the medium and small bodies K_b monotonically decreases to zero.

Figure 5 shows the curvature (the reciprocal of local radius of curvature, $1/|a|$) of streamlines for $-0.3 < x/R < 0.3$ at different radial locations. Only the results for the large body are shown, but for the small and medium bodies the variation of curvature is qualitatively the same but less dramatic. It is clear that the curvature effect is strong near the body surface (r small) and fades towards the pipe wall, and that a rapid switch from concave to convex curvature occurs near $x = 0$. In fact, the flow behavior in this region is even more complicated because, in addition to the curvature, there also exists a strong APG as the flow approaches the tip of the body. The combined deceleration and curvature effect poses an interesting question to the response of turbulence, for which we will gain some insights from our later discussion on the Reynolds shear stress. Further downstream ($0.3 < x/R < 2.67$, not shown here), the flow sees convex curvature with the magnitude decreasing in both the axial and radial directions.

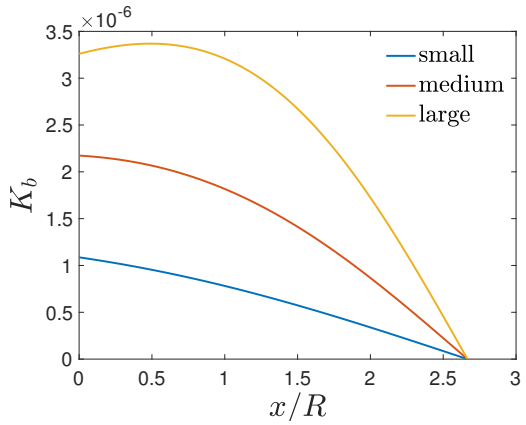

Figure 4: Acceleration factor K_b based on the bulk velocity.

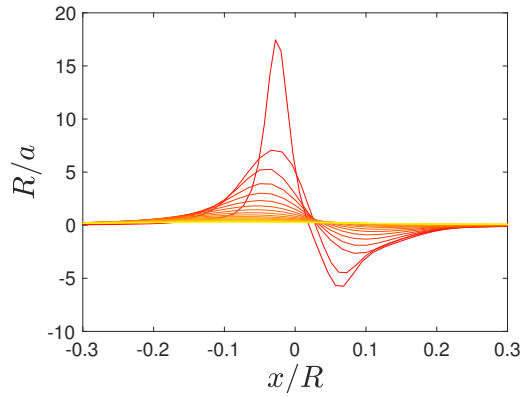

Figure 5: Curvature of streamlines near x = 0 of the large body at different radial locations, where r increases from red to yellow. Here, $|a|$ is the local radius of curvature ($a > 0$ and $a < 0$ represent concave and convex curvature, respectively).

Mean velocity

Figure 6 shows the mean velocity profiles in the streamline coordinate system, that is, U_s as a function of

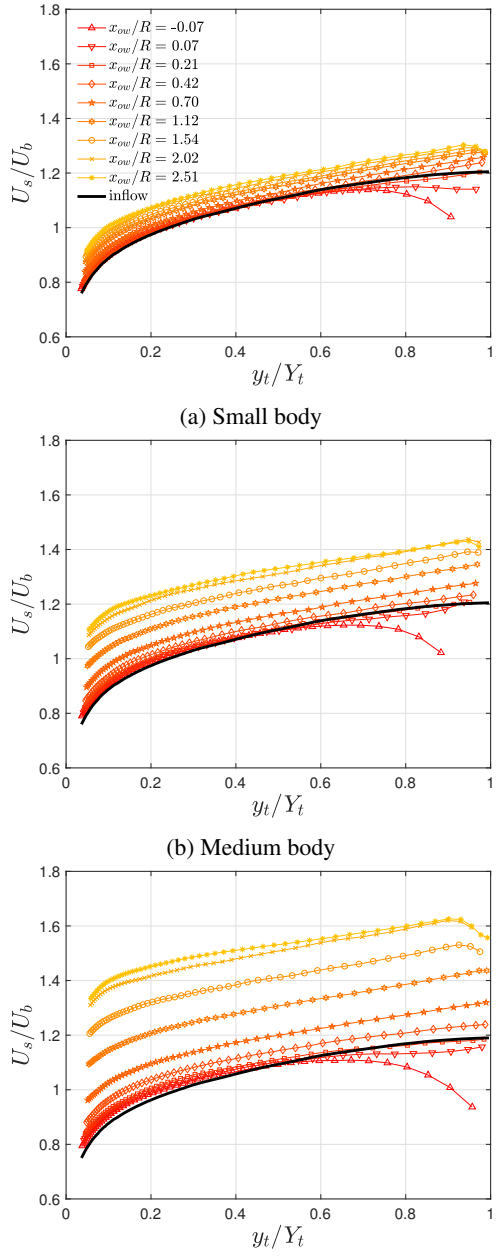

(a) Small body

(b) Medium body

(c) Large body

Figure 6: Profiles of U_s as functions of y_t/Y_t in the bow section ($x/R < 2.67$). The results are shown at different stations of x_{ow}/R, where x_{ow} is the x-coordinate where a potential line intersects with the pipe wall.

y_t/Yt. The results are displayed for the bow section ($x/R <$ 2.67) at multiple stations of x_{ow}/R, where x_{ow} is the x-coordinate of an intersection between a potential line and the pipe wall. The incoming fully developed velocity profile is also plotted for reference. As expected, the flow over the large body exhibits the strongest global acceleration. The evolution of mean velocity distributions for the three body sizes are qualitatively similar, despite the differences in the strengths of the pressure gradients and streamline curvature (c.f. figure 4 and 5). When the flow is approaching the body of revolution, the velocity near the pipe center is dramatically slowed down by the presence of the bow, as seen at $x_{ow}/R = -0.07$. Meanwhile the flow near the pipe wall (small y_t) speeds up to satisfy conservation of mass. The velocity increase near the pipe wall is much smaller compared to the decrease in the pipe center, since the central part of the pipe only occupies a very small fraction of the pipe cross section. After the flow passes the line of $x/R = 0$, the flow near the body surface quickly accelerates to catch up. As seen at x_{ow}/R = 0.07 for the medium and large bodies, the maximum U_s already occurs very close to the body surface ($y_t/Y_t > 0.95$) ; for the small body, this occurs only slightly later.

The flow then continues to accelerate, and the acceleration appears to be relatively uniform across $0.1 < y_t/Y_t <$ 0.9 from approximately x_{ow}/R = 0.3 to 2.0. Interestingly, we observe a linear law established away from the pipe wall. To confirm the existence of the linear region, we computed dU_s/dy_t and plot the result for the large body in figure 7 (the results for the small and medium bodies are similar). Compared to the continuously decreasing slope of the fully developed flow, the results clearly suggest a region of constant dU_s/dy_t starting from $y_t/Y_t \approx 0.5$. The linear region extends to at least $y_t/Y_t = 0.95$ up to $x_{ow}/R \approx 1.15$. Further downstream the linear region shortens as a result of the boundary layer development on the body wall. From our later discussion it will become evident that the linear distribution, as opposed to the lessening gradient in a fully developed flow, is due to the Reynolds shear stress redistributing the momentum.

Beyond $x/R = 2.67$, the flow starts the recovery process over the midbody region where the streamwise curvature and bulk acceleration become negligible. The velocity profiles in this range ($2.67 < x_{ow}/R < 5.50$) are presented in figure 8. Again, we see the behaviors of the mean velocity are qualitatively similar for the three body sizes but the

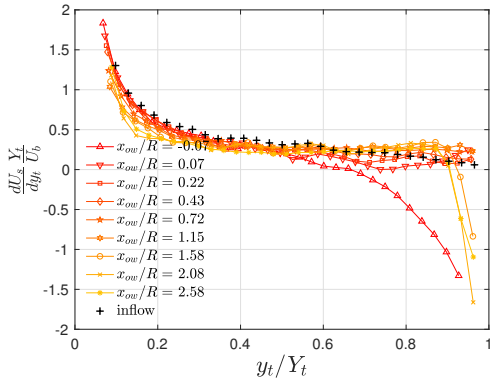

Figure 7: Profiles of the mean velocity gradient in the streamline coordinate system, dU_s/dy_t, showing the existence of linear region.

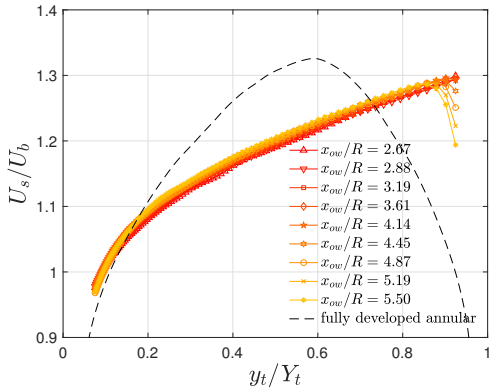

(a) Small body

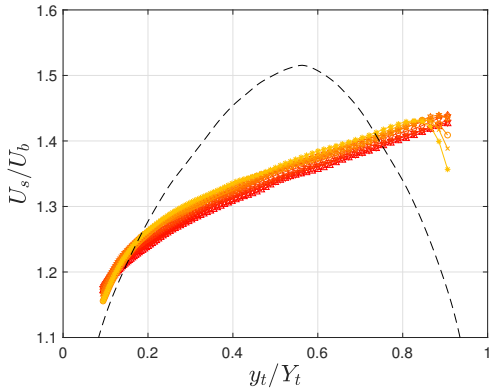

(b) Medium body

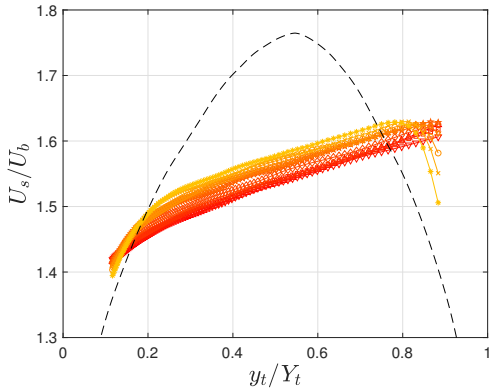

(c) Large body

Figure 8: Profiles of U_s as functions of y_t/Y_t in the recovery region ($2.67 < x/R < 5.50$). Black dashed lines are schematic distributions of fully developed annular flows based on Kaneda *et al.* (2003).

process takes place in a more pronounced way for the larger bodies. The velocity grows in the central part between the two walls, whereas the near-wall flow is retarded by the walls so that the low-momentum layers gradually thicken. For the large body, the velocity at $y_t/Y_t = 0.5$ grows by about 3%, and this growth for the small body is only about 1%. It is evident by the comparison in figure 8 that the flow is far from the equilibrium state which is a fully developed annular pipe flow. The recovery process is therefore expected to last for a long distance, well beyond our measurement domain.

The thickening of the boundary layers at both walls may be viewed as an analogy to the growth of a turbulent boundary layer absent mean pressure gradient. After the

flow exits the bow section, it loses a significant amount of driving force from the pressure differences. The net effect is that the flow only feels the retardation by the wall, and it slowly adjusts itself until the pressure gradient and the wall shear stress are balanced.

Reynolds shear stress

As indicated earlier, the Reynolds shear stress plays an important role in shaping the velocity distribution in the bow section. Shown in figure 9 is the Reynolds shear stress $-\overline{u_s' u_t'}$ for $-0.13 < x_{ow}/R < 1.20$, a range over which $-\overline{u_s' u_t'}$ undergoes a relatively dramatic change. The most notable result is the emergence of negative $-\overline{u_s' u_t'}$ near the body surface, as opposed to the fully developed flow having positive $-\overline{u_s' u_t'}$ across the pipe radius. We can gain some insights into the negative Reynolds shear stress by examining its production in the transport equation (presented in Cartesian form for convenience):

$$U\frac{\partial \overline{u'v'}}{\partial x} + V\frac{\partial \overline{u'v'}}{\partial y} = -\overline{u'^2}\frac{\partial V}{\partial x} - \overline{v'^2}\frac{\partial U}{\partial y} + \ldots \qquad (1)$$

Here, u and v are the velocity components in the s- and t-direction, respectively. Note that gradients in the azimuthal direction are zero, and also that $-\overline{u'v'}(\partial U/\partial x + \partial V/\partial y) = 0$ on the right side due to continuity. Close to the pipe center, as the flow approaches the body, $\partial U/\partial y$ is negative and large; $\partial V/\partial x$ is also negative and large due to strong streamline divergence. So the production on the right side is positive and significant, which means $-\overline{u'v'}$ decreases ($\overline{u'v'}$ increases) as a fluid particle moves along the mean streamline direction (U,V). As a result, $-\overline{u'v'}$ near the pipe centerline becomes negative, i.e. the momentum transfer is enhanced in this region. For the large body, the enhancement is more pronounced because of more significant $\partial U/\partial y$ and $\partial V/\partial x$ compared to the smaller bodies.

The energized turbulence then experiences the convex curvature and FPG near the body surface, both of which tend to attenuate the turbulence (Muck *et al.*, 1985; Harun *et al.*, 2013). This attenuation is expected to be the most severe for the largest body that provides the strongest curvature and FPG, but more high-resolution near-wall data is needed to confirm this expectation. The current data suggest the attenuation of $-\overline{u_s' u_t'}$ at $y_t/Y_t = 0.9$ is approximately $0.2u_\tau^2$ for all three cases. At the pipe wall, the FPG is the dominant mechanism suppressing the turbulence. The decrease in $-\overline{u_s' u_t'}$ over the largest body is found to be about twice that of the smallest body. The value of y_t/Y_t for zero shear stress is about 0.6 for the large body, 0.7 for the medium body, and 0.8 for the small body. In each case, this value tends to increase with x_{ow}/R as a result of decreasing turbulence intensity near the body wall.

The physical process associated with negative $-\overline{u_s' u_t'}$ is that, in an average sense, high momentum fluid moves towards the *body wall* and low momentum fluid moves towards the *pipe wall*. Note that in the region where $-\overline{u_s' u_t'} < 0$, $dU_s/dy_t > 0$. This is to say, the momentum transfer in this region enhances the velocity gradient. In addition, in the region where $-\overline{u_s' u_t'} > 0$, the momentum transfer happens in the same direction as in the fully developed pipe flow but less intensely. The end result is that the velocity profile in this region is less flattened compared to the fully developed flow. Therefore, the flow in the bow section maintains a high velocity gradient when y_t/Y_t increases,

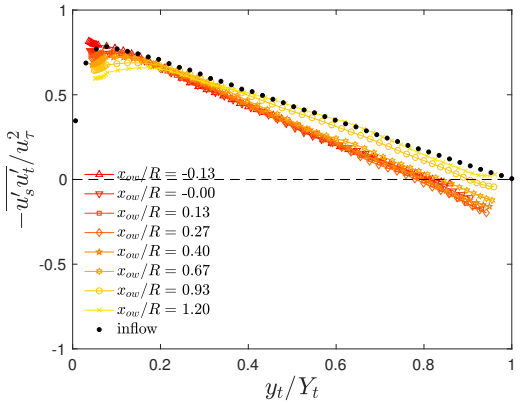

(a) Small body

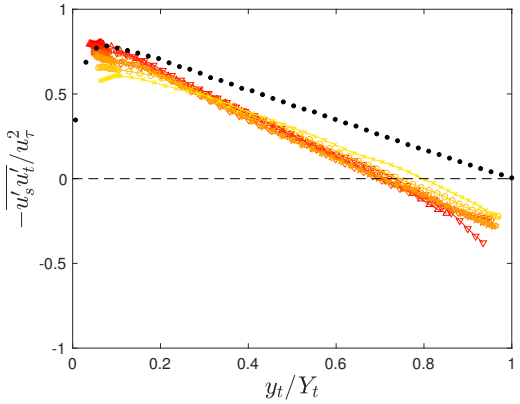

(b) Medium body

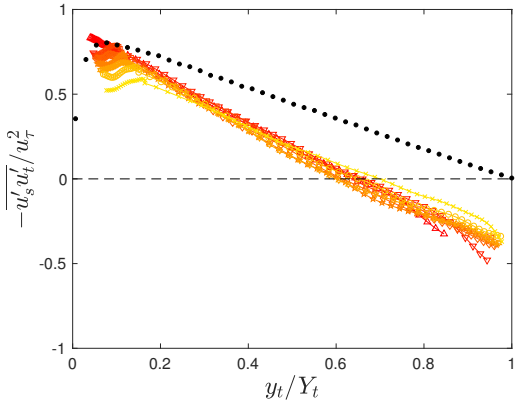

(c) Large body

Figure 9: Profiles of $-\overline{u_s' u_t'}$ as functions of y_t/Y_t in the bow section. Black dots represent the incoming fully developed flow. u_τ is the friction velocity of the upstream fully developed flow.

in contrast to the lessening gradient in the fully developed flow. This helps to explain the existence of the linear distribution observed in figure 6.

The Reynolds shear stress in the recovery section of the medium body is displayed in figure 10 (the results for the small and large bodies are qualitatively similar). The most noticeable change occurs near the walls as $-\overline{u_s' u_t'}$ is mostly produced in high-shear regions. However, for the most part the variation of $-\overline{u_s' u_t'}$ is very small, and it is far from the fully developed annular pipe flow. It is therefore reasonable to expect a long-lasting recovery process.

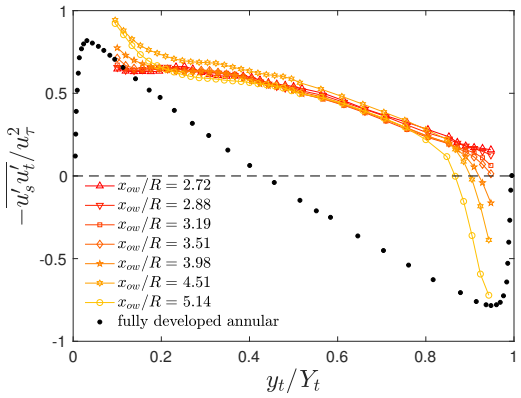

Figure 10: Profiles of $-\overline{u_s' u_t'}$ for the medium body in the recovery section ($2.72 < x_{ow}/R < 5.14$). The result of a fully developed annular pipe flow is based on Kaneda *et al.* (2003).

CONCLUSIONS

We investigated a turbulent pipe flow at $Re_D = 156,000$ passing over different bodies of revolution placed on the centerline. Each body had a streamlined shape introducing a favorable pressure gradient and convex streamline curvature to the flow over the bow section. The flow subsequently underwent recovery through a circular annulus formed by the pipe wall and the constant area mid-section of the body.

The mean streamwise velocity in the bow section exhibited a linear distribution in $0.5 < y_t/Y_t < 0.9$, a region above the overlap layer of the pipe wall. The linear distribution was observed over the major part of the bow section.

The production of Reynolds shear stress appeared to be responsible for the formation of the linear distribution of the mean velocity. We found strong negative $-\overline{u_s' u_t'}$ near the body wall at the beginning of the bow section, which strengthened the velocity gradient to form the linear distribution, as opposed to the velocity gradient of the equilibrium flow which continuously decreases towards the pipe center.

The strong negative $-\overline{u_s' u_t'}$, which indicated energized turbulence, resulted from the strong deceleration and streamline divergence prior to the bow tip. We analyzed the transport equation of $-\overline{u_s' u_t'}$ to explain the strong production of Reynolds shear stress in this region.

In midbody recovery section, the flow underwent a slow recovery process. The variation near the walls were more pronounced, but overall the flow only changed slightly. The recovery process was therefore expected to continue for a long distance.

Acknowledgments

The authors gratefully acknowledge the support under ONR Grant "Understanding Turbulence on Navy Vehicles" N00014-17-1-2309 (Program Manager Joseph Gorski).

REFERENCES

Agüera, N., Cafiero, G., Astarita, T. & Discetti, S. 2016 Ensemble 3D PTV for high resolution turbulent statistics. *Measurement Science and Technology* **27** (12), 124011.

Fuchs, T., Hain, R. & Kähler, C. J. 2017 Non-iterative double-frame 2D/3D particle tracking velocimetry. *Experiments in Fluids* **58** (9), 119.

Harun, Z., Monty, J. P., Mathis, R. & Marusic, I. 2013 Pressure gradient effects on the large-scale structure of turbulent boundary layers. *Journal of Fluid Mechanics* **715**, 477–498.

Hoffmann, P. H., Muck, K. C. & Bradshaw, P. 1985 The effect of concave surface curvature on turbulent boundary layers. *Journal of Fluid Mechanics* **161**, 371–403.

Kähler, C. J., Scharnowski, S. & Cierpka, C. 2012 On the uncertainty of digital PIV and PTV near walls. *Experiments in Fluids* **52** (6), 1641–1656.

Kaneda, M., Yu, B., Ozoe, H. & Churchill, S. W. 2003 The characteristics of turbulent flow and convection in concentric circular annuli. Part I: Flow. *International Journal of Heat and Mass Transfer* **46** (26), 5045–5057.

McKeon, B. J., Swanson, C. J., Zagarola, M. V., Donnelly, R. J. & Smits, A. J. 2004 Friction factors for smooth pipe flow. *Journal of Fluid Mechanics* **511**, 41–44.

Monty, J. P., Harun, Z. & Marusic, I. 2011 A parametric study of adverse pressure gradient turbulent boundary layers. *International Journal of Heat and Fluid Flow* **32** (3), 575–585.

Moonesun, M., Korol, Y. M., Dalayeli, H., Tahvildarzade, D., Javadi, M., Jelokhaniyan, M. & Mahdian, A. 2017 Optimization on submarine stern design. *Proceedings of the Institution of Mechanical Engineers, Part M: Journal of Engineering for the Maritime Environment* **231** (1), 109–119.

Muck, K. C., Hoffmann, P. H. & Bradshaw, P. 1985 The effect of convex surface curvature on turbulent boundary layers. *Journal of Fluid Mechanics* **161**, 347–369.

Nagano, Y., Tagawa, M. & Tsuji, T. 1993 Effects of adverse pressure gradients on mean flows and turbulence statistics in a boundary layer. In *Turbulent Shear Flows 8*, pp. 7–21. Springer.

Nagib, H. M. & Chauhan, K. A. 2008 Variations of von Kármán coefficient in canonical flows. *Physics of Fluids* **20** (10), 101518.

Saxton-Fox, T., Ding, L., Smits, A. J. & Hultmark, M. 2019 Coherent structure deformation in a turbulent pipe flow with a spatially-developing pressure gradient. In *Proc. Turbulence and Shear Flow Phenomena 11*. University of Southampton, Southampton, UK.

Smits, A. J., Ding, L. & Van Buren, T. 2019 Flow over a square bar roughness. In *Proc. Turbulence and Shear Flow Phenomena 11*. University of Southampton, Southampton, UK.

Smits, A. J., Young, S. T. B. & Bradshaw, P. 1979 The effect of short regions of high surface curvature on turbulent boundary layers. *Journal of Fluid Mechanics* **94** (2), 209–242.

Spalart, P. R. & Watmuff, J. H. 1993 Experimental and numerical study of a turbulent boundary layer with pressure gradients. *Journal of Fluid Mechanics* **249**, 337–371.

Van Buren, T., Hellström, L. H. O. & Smits, A. J. 2019 Turbulent pipe flow response to rough-to-smooth step change in roughness: Flow structure. In *Proc. Turbulence and Shear Flow Phenomena 11*. University of Southampton, Southampton, UK.